# Linear gyrokinetic simulations of Toroidal Alfvén Eigenmodes in the Mega-Amp Spherical Tokamak

H.H. Wong,[1] H. Huang,[2] P. Liu,[2] Y. Yu,[2] X. Wei,[2] G. Brochard,[3] N. Fil,[4] Z. Lin,[2] M. Podesta,[5] P.J. Bonofiglo,[6] K.G. McClements,[4] C.A. Michael,[1] N.A. Crocker,[1] L. Garzotti,[4] and T.A. Carter[7]

[1)] *University of California, Los Angeles*
[2)] *University of California, Irvine*
[3)] *ITER organization*
[4)] *United Kingdom Atomic Energy Authority, Culham Campus, Abingdon, Oxfordshire OX14 3DB, United Kingdom*
[5)] *Ecole Polytechnique Federale de Lausanne*
[6)] *Princeton Plasma Physics Laboratory*
[7)] *Oak Ridge National Laboratory*

(*Electronic mail: henry.h.wong@physics.ucla.edu)

(Dated: 12 September 2024)

Linear gyrokinetic (GK) simulations using the Gyrokinetic Toroidal Code (GTC)[1] have been performed to investigate Toroidicity-driven Alfvén Eigenmodes (TAEs) driven by neutral beam injection (NBI) induced fast ions in the Mega-Amp Spherical Tokamak (MAST) to identify the non-perturbative and kinetic effects of thermal plasmas. A specific TAE in MAST discharge 26887, with on-axis NBI power of approximately 1.5 MW and plasma current around 800 kA, exhibited frequency chirping, and the tangential soft X-ray (SXR) camera array resolved radial mode structure peaked near $|q| = 1.5$. Various excitation methods were used in the GTC linear simulations, illustrating this code's capability to realistically represent the mechanisms and behaviors of fast ion-driven TAEs in spherical tokamaks. The radial structures from these GK simulations closely match measurements and calculations performed using the NOVA ideal MHD code, though with frequencies approximately 10 kHz lower, likely due to various kinetic and non-perturbative effects. The simulations measured the damping rates due to continuum damping, radiative damping, and ion Landau damping, revealing that ion Landau damping has the most significant contribution to the total damping rate of the TAE. A comparison of growth rates of TAEs excited by fast ion Maxwellian and slowing-down distributions shows that the TAEs excited by a fast ion anisotropic pitch distribution (as part of the slowing-down distributions) are more unstable compared to those excited by a Maxwellian distribution with a equivalent fast ion beta. This shows that the use of fast ion anisotropy alters the amount of fast ions to be in shear Alfvén resonance, and hence it can greatly affect the stability of TAEs.

## I. INTRODUCTION

Neutral beam injection (NBI) is one of several sources of fast ions in tokamaks that can induce instabilities leading to significant fast ion transports or losses, threatening both heating efficiency and plasma-facing components' integrity[2]. Consequently, the development of simulations capable of accurately modeling these instabilities and their associated fast ion transports is essential for the success of future fusion tokamaks. Linear MHD models are often used to simulate modes excited in tokamaks by fast ions, including those arising from NBI[3]. However, to capture kinetic effects of thermal plasma at microscopic scale that could affect the instability-induced fast-ion transport, it is appropriate to use a kinetic description for both the thermal plasma and the fast ions.

Global gyrokinetic (GK) codes, such as the Gyrokinetic Toroidal Code (GTC), offer promising capabilities for cross-scale integrated simulations of fast particle-driven modes[4]. However, these codes must be validated through comparisons with other simulation models and experimental measurements. GTC has been benchmarked against ideal and resistive MHD, as well as other GK simulations, for toroidicity-induced Alfvén eigenmodes (TAEs) and reversed shear Alfvén eigenmodes (RSAEs) in conventional tokamaks like DIII-D[567]. However, investigations into TAEs in spherical tokamaks (STs) using global GK simulations remain notably rare and unreported compared to studies using ideal MHD models. In addition to differences in aspect ratio, the ratio of fast ion beta ($\beta_{FI}$) to thermal ion beta ($\beta_i$) is typically much higher in some STs, such as the Mega-Amp Spherical Tokamak (MAST)[8], compared to conventional tokamaks. Global GK simulations have not yet been conducted in this $\beta_{FI}$ regime.

This paper aims to bridge this gap by comparing the results of linear GTC and ideal MHD simulations of a TAE in MAST to identify the non-perturbative and kinetic effects of thermal plasma. New experiments dedicated to TAEs are planned for MAST-U (the upgraded version of MAST)[9] and provide opportunities for model validations. For example, there is an ongoing effort to investigate the damping channels of n = 3 TAEs in MAST-U using ORB5 (another GK model)[10], but without the use of fast ion anisotropy. However, MAST presents a simpler NBI configuration that is more straightforward for modeling fast ion anisotropy in GTC, which is the first time to be used in a GK simulation of fast ions driven AEs in a ST. In addition, global radial mode structure measurements from tangential soft X-ray cameras were were accessible in MAST, but they were unavailable during in the early physics campaigns in MAST-U. These factors make the targeted TAE case in MAST more suitable for model validation compared

to cases from MAST-U.

The remainder of this paper is organized as follows. The underlying formulation of GTC is first compared with hybrid GK-MHD and ideal MHD models in the long wavelength limit (Section II). The experimental parameters and measurements of the targeted TAE case are presented in Section III. The frequency and spatial mode structure of the TAE computed using the ideal MHD code NOVA[11] (Section IV) are compared with those of the modes excited by an antenna in GTC, along with calculations of damping rates due to continuum damping, radiative damping, ion Landau damping, and finite Larmor radius (FLR) effects (Section V; cases I - IV in Table I). Additionally, TAEs are driven by Maxwellian and anisotropic slowing-down fast ion distributions in linear GTC simulations to examine the effects of these different types of drive on mode structure, frequency, and growth rate (Section VI; cases V - VI in Table I).

## II. GTC GYROKINETIC FORMULATIONS AND ITS REDUCTION TO IDEAL MHD

The Gyrokinetic Toroidal Code (GTC) employs a gyrokinetic particle-in-cell (PIC) method to handle both thermal and fast ions, but can also be operated using reduced models including a fluid-kinetic electron hybrid model, a two fluid model, and a single fluid model. The gyrokinetic equation (Equation 2 in[12]) is used to describe toroidal plasmas in the inhomogeneous magnetic field[13] with the gyrocenter position, magnetic moment $\mu$, and parallel velocity $v_{||}$ as independent variables. The distribution functions of different species can be decomposed into equilibrium ($f_{0i}$) and perturbed ($\delta f_i$) parts. Although this work solely focuses on linear perturbative simulations, GTC is capable of handling non-linear evolution of full-f and $\delta f$ distributions. In the fluid-kinetic electron hybrid model, electron distribution function is expanded into an adiabatic part (calculated by a fluid equation) and non-adiabatic part (calculated by the PIC method). The fluid continuity equation describes the electrons as a massless fluid, and the non-adiabatic part of the electron distribution function defines the electron kinetic effects. The equilibrium distributions of thermal electrons and ions are described as Maxwellian distributions, while either Maxwellian or analytic slowing-down distributions can be used to describe the fast ions. The zonal and non-zonal perturbed electrostatic potentials ($\phi_{00}$ and $\delta\phi$, respectively) are obtained by solving the gyrokinetic Poisson's equation[7]. The parallel electric field is defined as

$$\delta E_{||} = -\mathbf{b_0}\cdot\nabla\phi_{eff} \tag{1}$$

, where $\mathbf{b_0} = \mathbf{B_0}/|B_0|$, and the effective electrostatic potential $\phi_{eff}$ contributes to the inductive potential $\phi_{ind} = \phi_{eff} - \delta\phi$. Subsequently, the perturbed parallel vector potential can be calculated by:

$$\partial_t \delta A_{||} = \mathbf{b_0}\cdot\nabla\phi_{ind} \tag{2}$$

The inclusion of $\phi_{eff}$ results in a model similar to a hybrid GK-MHD model discussed in[14] and[15] but with the addition of pressure-driven terms. This model can be further reduced to ideal MHD by setting $\delta E_{||} = 0$, resulting in the exact formulation shown in Equation (53) in[7], which includes terms that describe the bending of field lines responsible for shear Alfvén modes, current-driven modes such as the kink mode, and pressure-driven instabilities. A notable distinction between the hybrid GK-MHD model and the ideal MHD model lies in the inclusion of $\delta E_{||}$. A parallel electric field can lead to particle acceleration, alter the shear wave dispersion relation[16], and introduce additional damping compared to the ideal MHD regime without parallel electric fields.

GTC offers different run modes to explore various growth and damping mechanisms by treating the $\phi_{ind}$ and the gradient of fast ion distributions differently. The $\delta A_{||}$ and $\delta\phi$ perturbations defined above are used in the gyrokinetic particle weight ($w_i = \delta f_i/f_i$) equation that handles the evolution of perturbed distribution functions, rewritten as the following:

$$\frac{dw_i}{dt} = (1-w_i)\left[-(v_{||}\frac{\delta\mathbf{B}}{B_0}+v_E)\cdot\frac{\nabla f_{0i}}{f_{0i}}|_\mu + \left(\mu\frac{\delta\mathbf{B}}{B_0}\cdot\nabla B_0 + eZ_i\frac{\mathbf{B}^*}{B_0}\cdot\nabla\delta\phi + eZ_i\partial_t\delta A_{||}\right)\left(\frac{1}{m_i f_{0i}}\frac{\partial f_{0i}}{\partial v_{||}}\right)\right] \tag{3}$$

, where $i$ is the species, $v_E$ is the $E\times B$ drift velocity, $\mathbf{B}$ is the total magnetic field, $\mathbf{B}^*$ is related to $\mathbf{B}$ (defined in[12]), and $eZ_i$ is the effective charge of the species. Some of the quantities in the weight equation will be handled differently to test various physics regimes. For instance, the code provides the option of turning finite $\delta E_{||}$ on and off by treating $\partial_t\delta A_{||}$ differently in the two- and single-fluid ideal MHD run modes, respectively, to test continuum and radiative damping mechanisms separately. Ion Landau damping can also be added on top of these damping mechanisms when the thermal ions are in the gyrokinetic regime.

GTC incorporates thermal ion temperature and density profiles into Maxwellian distributions in the simulations that consider gyrokinetic thermal ions. The Maxwellian distribution is defined as follows:

$$f_{0a} = \frac{n_{0a}}{(2\pi T_{0a}/m_i)^{3/2}} exp\left(-\frac{2\mu B_0 + m_a v_{||}^2}{2T_{0a}}\right) \tag{4}$$

, where the subscript $a$ represents the species, and $n_{0a}$, $T_{0a}$, and $m_a$ represent the species' density, temperature, and mass, respectively, with $B_0$ being the equilibrium magnetic field. The gyrokinetic weight equation (Equation 3) shows that the mode structure depends on the gradients of the distributions ($\nabla f_{0a}/f_{0a}$ and $(1/f_{0a})(\partial f_{0a}/\partial v_{||})$) defined as:

$$\frac{\nabla f_{0a}}{f_{0a}}|_\mu = \left(\frac{1}{n_{0a}}\frac{\partial n_{0a}}{\partial\psi} - \frac{3}{2T_{0a}}\frac{\partial T_{0a}}{\partial\psi}\right)\nabla\psi - \frac{\mu}{T_{0a}}\nabla B_0 \tag{5}$$

| case | description | damping/driving mechanisms | eigen-frequency (kHz) without Doppler shift | $\gamma_{tot}/\omega$ (%) |
|---|---|---|---|---|
| I | single-fluid MHD | antenna, continuum | 70.1 | -4.77 |
| II | two-fluid MHD (with $\delta E_{\|\|}$) | case I + radiative | 72.0 | -5.97 |
| III | full-kinetic thermal ions (without gyro-averaging) | case II + ion Landau | 69.2 | -11.0 |
| IV | gyro-kinetic thermal ions (with gyro-averaging) | case III + FLR | 69.3 | -10.8 |
| V | gyro-kinetic thermal + fast ions (Maxwellian distribution) | case IV without antenna + with fast ion gradient drive | 69-72 (Figure 9(b)) | 3.6 - 11.8 (Figure 9(a)) |
| VI | gyro-kinetic thermal + fast ions (slowing down distribution) | case IV without antenna + with fast ion gradient drive | 66 (Figure 9(b)) | 10.8 (Figure 9(a)) |

TABLE I. Various simulation cases to measure the mode eigen-frequencies and total growth/damping rates with different combinations of damping and driving mechanisms of the n = 1 TAE located near the q = 1.5 surface

and

$$\frac{1}{f_{0a}}\frac{\partial f_{0a}}{\partial v_{||}} = -\frac{m_a v_{||}}{T_{0a}} \tag{6}$$

, respectively.

Fast ions can also be included in GTC to excite modes. These fast ions can be represented by a Maxwellian distribution, similar to the treatment of thermal ions (Equation 4), or by an analytic fast ion slowing-down distribution[17], defined as:

$$f_{0f} = \frac{n_{0f}H(v_0-v)}{v^3+v_c^3} exp\left(-\left(\frac{\lambda-\lambda_0}{\Delta\lambda}\right)^2\right) \tag{7}$$

Here $f$ is the label for the species, which in this case is just for the fast ions from a single NBI injection while the thermal species are still represented by the Maxwellian distribution (Equation 4). $v = \sqrt{v_{||}^2 + 2\mu B_0/m}$ where $v_{||}$ is the parallel velocity of the particles, $v_c = v_{c,0}\sqrt{T_f/m_f}$ is the critical velocity (where $v_{c0}$ is a dimensionless scale factor), $v_0 = v_{0,0}\sqrt{T_f/m_f}$ is the birth velocity (where $v_{0,0}$ is a dimensionless scale factor), $H$ is the Heaviside step function, $\lambda = \mu B_0/E$ is related to the pitch of the particle with respect to the on-axis magnetic field $B_0$, $E$ is the fast ion's kinetic energy, $\lambda_0$ is a constant associated with the birth pitch, and $\Delta\lambda$ is the width of the pitch angle distribution. The gradients of the analytic slowing-down fast ion distribution ($\nabla f_{0f}/f_{0f}$ and $(1/f_{0a})(\partial f_{0a}/\partial v_{||})$ ) are given by:

$$\frac{\nabla f_{0f}}{f_{0f}}|_\mu = \left(\frac{1}{n_{0f}}\frac{\partial n_{0f}}{\partial \psi} - \frac{3v_c^3}{2(v^3+v_c^3)T_f}\frac{\partial T_{0f}}{\partial \psi}\right)\nabla\psi$$

$$+\left(\frac{2\lambda^2}{B_a\Delta\lambda^2}(\lambda-\lambda_0) - \frac{1}{m_f}\frac{3\mu v}{v^3+v_c^3}\right)\nabla B_0 \tag{8}$$

and

$$\frac{1}{f_{0a}}\frac{\partial f_{0a}}{\partial v_{||}} = \frac{2m_a v_{||}\lambda^2}{\mu B_0\Delta\lambda^2}(\lambda-\lambda_0) - \frac{3vv_{||}}{v^3+v_c^3} \tag{9}$$

, respectively. These gradients determine the mode structure when an analytic slowing-down fast ion distribution is considered.

## III. MAST TEST CASE: EXPERIMENTAL PROFILES AND TAE MEASUREMENTS

MAST plasma discharge 26887 was selected for analysis. This device had a major radius $R_0 \approx 0.9$ m and a minor radius $a \approx 0.6$ m. Notably, the $a/R_0$ ratio for MAST ( $\approx 0.66$) is considerably larger than that of many conventional tokamak cases (e.g., $a/R_0 \approx 0.333$ for JET[18]), which are typically used to validate and benchmark GTC simulations. The plasma current is approximately 800 kA and the toroidal field on the magnetic axis is around 0.43 T.

The mode frequency and radial structure of a TAE-like burst at $t \approx 180$ ms with toroidal mode number $n = 1$ in discharge 26887 are inferred from various diagnostics. Core-localized, large-scale, low-frequency instabilities are typically readily detected by a toroidally extended Mirnov coil array (OMAHA)[19], owing to its high signal-to-noise ratio. The toroidal mode numbers (n) were identified for each time and frequency using a Singular Value Decomposition (SVD)-based method[20]. The selected $n = 1$ burst begins at a frequency of approximately 90 kHz and then chirps down to around 65 kHz (in the lab frame) in approximately 2 ms, as shown in figure 1 (a). The core plasma rotation frequency is about 10kHz, meaning the mode frequency is about 10kHz lower from the measurement in the plasma frame. The electron density and temperature are measured using a Thomson scattering diagnostic, showing increases in both core electron density and temperature (taken at R = 1.0m) over the period of the appearance of TAEs in figure 1 (b) and (c). Plasma heating is provided by an on-axis mid-plane NBI, the power increasing from 1.0MW to approximately 1.6MW at 170ms, as shown in figure 1 (d). The neutron emission inferred from fission chamber measurement increases slowly over time after 180ms (shown in figure 1 (e)) in the presence of a steady NBI power input.

The safety factor (q) profile and the TAE radial structure are also inferred or reproduced from various diagnostics and calculations. The $q$ profile and magnetic configuration are reproduced from the MSE constrained EFIT++ reconstruction[21,22,23], with minimum safety factor $|q_{min}| = 1.23$ at the flux surface of $\rho = \sqrt{\psi_{pol}} \approx 0.45$ and central safety factor $|q_0| = 1.4$ at $t \approx 180$ms (shown in figure 2 (b)), which

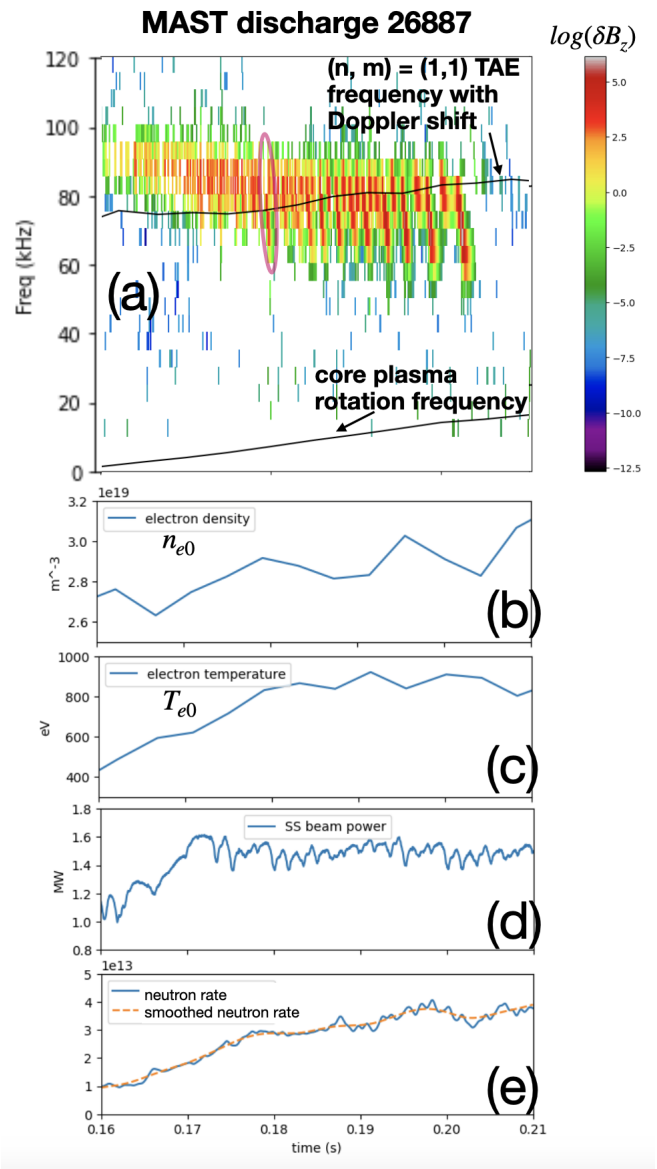


FIG. 1. (a) MAST discharge 26887 $\delta B_z$ spectrogram with the targeted TAE circled in pink, (n,m) = 1,1 TAE frequency and core plasma rotation frequency labeled in black lines; core (at R = 1.0m) electron (b) density and (c) temperature from Thomson scattering; (d) NBI power; (e) total neutron emission from fission chamber, and low pass filtered (DC) neutron emission showing the slow evolving part of the total neutron emission

is the time of the selected TAE-like burst. The radial structure of that burst is inferred from tangential Soft X-ray (SXR) cameras[24]. The beam emission spectroscopy diagnostic that measures electron density fluctuations ($\delta n_e/n_{e0}$) was not yet available when the experiment was conducted, and electron cyclotron emission imaging (ECEI), that measuring electron temperature fluctuations ($\delta T_e/T_{e0}$) could not be implemented in MAST due to the low magnetic field strength. Hence the SXR camera array provided the most viable option for measuring the global spatial structure of TAEs in this pulse. The methods of analysis (e.g. band-pass filters) and inversion of SXR line-integrated signals to obtain local emissivity can be found in H.H. Wong et al. NF 2024[25]. The inverted SXR emissivity fluctuation is represented as a linear combination of $\delta n_e/n_{e0}$ ,$\delta T_e/T_{e0}$ and $\delta Z_{eff}/Z_{eff,0}$:

$$\frac{\delta\varepsilon}{\varepsilon_0} = 2\frac{\delta n_e}{n_{e0}} + \left(\frac{1}{2} + \frac{E_{\text{photon}}}{T_{e0}}\right)\frac{\delta T_e}{T_{e0}} + \frac{\delta Z_{\text{eff}}}{Z_{\text{eff},0}} \tag{10}$$

Here $E_{\text{photon}}$, the lowest SXR photon energy that can be detected, is about 1keV in MAST[26], and $Z_{eff,0}$ is the equilibrium effective ion charge state, which is influenced by the densities of impurities. $Z_{eff,0}$ is usually less than 1.5 in the core region[27], meaning there are only low concentrations of impurities in the core. Therefore, the contribution of the fluctuation of effective charge ($\delta Z_{\text{eff}}/Z_{eff,0}$) to the SXR fluctuation is expected to be small, and negligible in the core. Expressing $\delta n_e/n_{e0}$ and $\delta T_e/T_{e0}$ in terms of plasma displacement $\xi$ using the linearized electron continuity and energy equations gives:

$$\frac{\delta n_e}{n_{e0}} = -\nabla\cdot\xi - \xi\cdot\frac{\nabla n_{e0}}{n_{e0}} \quad \& \quad \frac{\delta T_e}{T_{e0}} = -(\gamma-1)\nabla\cdot\xi - \xi\cdot\frac{\nabla T_{e0}}{T_{e0}} \tag{11}$$

Here, $\gamma$ represents the adiabatic index or ratio of specific heats for the electron fluid. For low-frequency modes, $T_e$ is typically assumed to be constant along field lines, leading to $\gamma = 1$. An approximation $\nabla\cdot\xi \approx 0$ can be made if we consider the compressional component of TAE to be small. Consequently, $\delta x/x_0 \approx -\xi\cdot\frac{\nabla x_0}{x_0}$ for both $x = n_e$ and $x = T_e$. This shows that the SXR emissivity fluctuation is closely related to radial plasma displacement. This quantity is commonly used for expressing TAE mode structure in various models (e.g. NOVA) because it fully characterizes incompressible modes in ideal MHD. The radial profile of the inferred TAE-associated emissivity fluctuation ( $\delta\varepsilon/\varepsilon_0$, as in eq.10 ) peaks at $\rho \approx 0.65$, where $|q| \approx 1.5$ on the outboard (low field) side, as shown in figure 2 (a). It is worth noting that the emissivity fluctuation is weaker on the inboard (high field) side than on the outboard side, indicating that the measured mode has a ballooning-like structure, which is common for TAEs with frequencies near the bottom of the n = 1 TAE continuum gap[28].

The selected MAST discharge is studied through GK simulations using the GTC code, as well as ideal MHD simulations using the eigenvalue NOVA code[11], along with the single-fluid ideal MHD feature integrated within GTC. Temperature and density profiles for thermal electrons and ions used for the simulations (shown in figure 3) are obtained from interpretive TRANSP[29] utilizing experimental data (Thomson scattering and carbon charge exchange recombination spectroscopy), while the magnetic configuration utilized in the simulations is obtained from MSE and pressure constrained EFIT++, as mentioned previously. Fast ion profiles are modeled using the NUBEAM[30] module of TRANSP. The two-dimensional (R,Z) fast ion density profile lacks radial and poloidal symmetry (as explained in Appendix A). Hence the GTC runs that have the modes excited by fast ions use NUBEAM results on the outboard (low field) side and at $\rho > 0.3$ only as the reference for analytic fast ion density and temperature profile inputs to provide sufficient fast ion gradients for driving TAE-like modes.

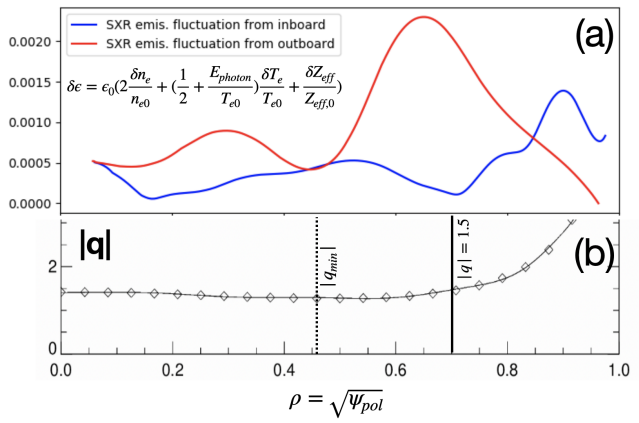


FIG. 2. (a) inverted SXR emissivity fluctuations and (b) |q| profile associated with the targeted TAE in MAST pulse 26887

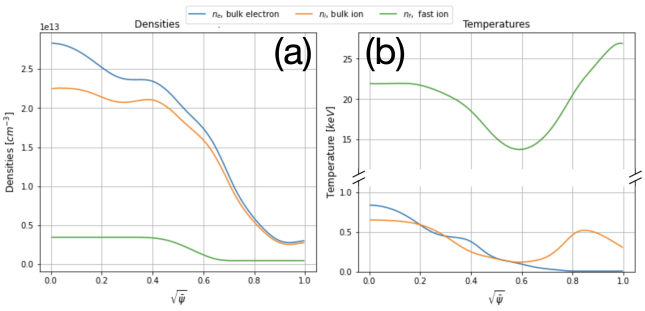


FIG. 3. (a) radial density and (b) temperature profiles from NUBEAM/TRANSP from thermal ions, electrons and fast ions used in GTC simulations.

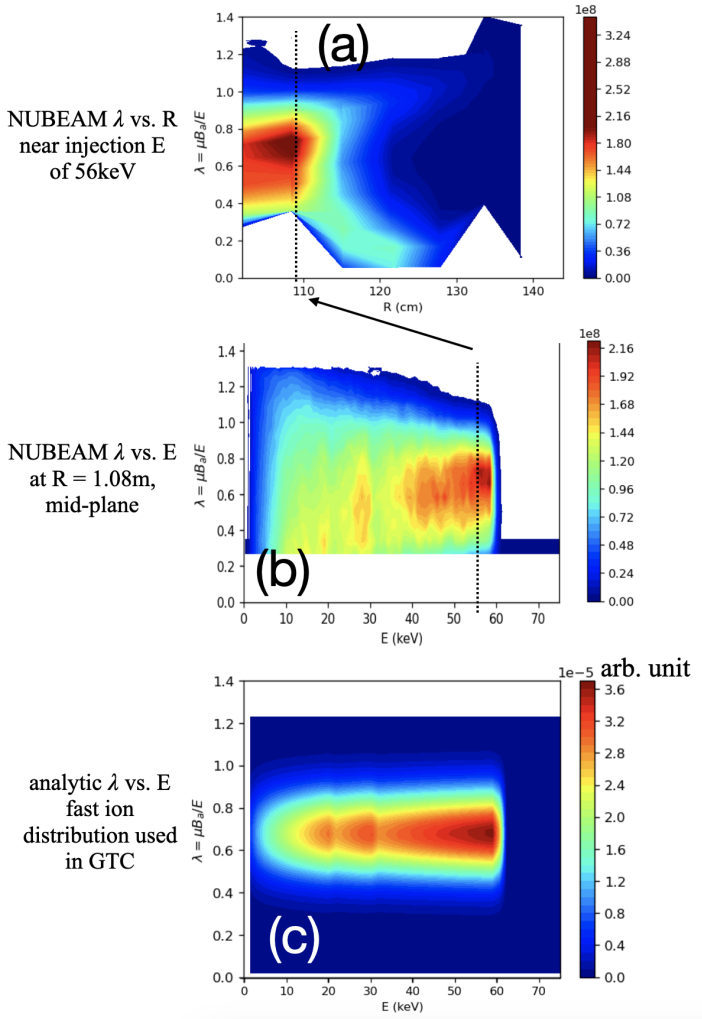


FIG. 4. fast ion distribution from NUBEAM calculated for MAST pulse 26887, t = 180ms. (a) $\lambda$ vs. R near injection energy; (b) $\lambda$ vs. E at (R,Z) = 1.08m,0.01m; (c) the analytic fast ion slowing-down distribution used in a linear GTC run, mimicking the injection $\lambda$ and three birth energies apparent in the distribution shown in (b)

Notably, the fast ions are significantly hotter (more than 20 times) and roughly one-fifth as dense as the thermal ions in the core. Hence the maximum fast ion beta ($(\beta)_{max} \propto (n*T)_{max}$) is about 5 times higher than the maximum thermal beta in the core. This regime was rarely investigated using global GK simulations previously. The NUBEAM calculation also provides slowing-down fast ion distributions in pitch and energy. Initially, fast ions generated by NBI concentrate near injection energy and pitch, undergoing slowing down, diffusion, and scattering through collisions and diffusion with the electrons and ions in a thermal background plasma[31323317]. The resulting slowing-down distribution retains most fast ions near their birth pitch at three energy levels. NUBEAM accounts for the geometries of NBI and the tokamak, determining the birth pitch angle of fast ions at different radii. Although fast ions are born within a relatively short segment of the beam line, this segment becomes significant in compact spherical tokamak pulse like the one in MAST presented here. Consequently, the birth pitch changes rapidly, from $\mu B_0/E \approx 0.6$ at $R \approx 1.1$ m near the location of peak fast ion density, to $\mu B_0/E \approx 0.15$ at $R \approx 1.3$ m near the $q = 1.5$ surface, as shown in Figure 4.

All GTC simulations, including single-, two-fluid ideal MHD and GK simulations employing various methods to excite the mode, have nearly identical simulation parameters (except for slight modifications to the boundary settings) to ensure consistency. The TAE simulations using antenna excitation have the inner boundary set to $\rho = 0.1$, and simulations that include fast ion distributions have the inner boundary set to about $\rho = 0.2$. The region beyond $\rho = 0.9$ up to the last closed flux surface (LCFS) is also excluded in all simulations. Radial linear decays near the inner and outer boundaries of the simulation perimeter are applied. These boundary settings have been carefully selected from a series of GTC test runs with the lowest levels of numerical instabilities among the test runs to mitigate their effects on accurately measuring the mode characteristics. The GTC simulations exclusively incorporate $n = 1$ and $m \in [0,7]$ modes, which should sufficiently account for the dominant harmonics of the low frequency $n = 1$ TAE.

## IV. CONTINUUM AND NOVA SIMULATIONS OF THE MAST TAE TEST CASE

The Alfvén continuum is computed using the continuum modules bundled with NOVA and GTC, as shown in figure 5. Unlike the NOVA code, the GTC in $\delta f$ run mode itself does not calculate the continuum directly. Instead it uses a bundled ALCON module[6] to solve ideal MHD Alfvén continua in tokamaks with the provided inputs for GTC. Comparing these continua is crucial to ensure similarity in inputs used by NOVA and GTC, in view of the differences in the treatment of magnetic configurations and equilibrium conditions, as mentioned previously. Additionally, the continuum provides insights into the TAE mode frequency and radial structure.

Generally, the continua from NOVA and single-fluid GTC align well with each other, exhibiting an $n = 1$ TAE gap ranging from about 80 to 130 kHz at $\rho = 0.2$, and widen to a range from 60 to 200 kHz at $\rho = 0.5$. The TAE gap in the targeted MAST case is notably broader than in conventional tokamaks due to the low aspect ratio[28]. Discrepancies arise near the edge ($\rho > 0.8$) in the part of the continuum associated with higher m harmonics, probably due to the different approaches employed by the two codes in handling equilibrium conditions. For example, the lower continuum at the bottom of the TAE gap from NOVA drops below a much lower frequency near $\rho = 0.82$ compared to GTC, possibly due to differences in the pressure models used by the two continuum modules. However, the targeted TAE likely has low m numbers with their widths of the $m \leq 2$ harmonics (interpreted by the full-width half-maximum of the radial structures) stay within $\rho < 0.85$. In addition, the region beyond $\rho = 0.9$ is excluded in GTC. Hence the discrepancies are unlikely to significantly impact the low-mode-number ($m \in [0,2]$) TAEs found in the simulations.

The NOVA code handles the magnetic configuration and plasma thermal profiles slightly differently from GTC. The code samples the region either above or below the mid-plane and assumes up-down symmetry in the magnetic configuration. The actual magnetic configuration, inferred from MSE-constrained EFIT++, indicates a slight up-shift of the magnetic axis by less than 3 cm at $t \approx 180$ ms. Consequently, the lower region is selected to avoid issues from the axis location. The NOVA simulations encompass $n = 1$ and $m \in [0,19]$ modes. Like GTC, solutions from NOVA are sometimes contaminated by instabilities. For example, these instabilities arise when a mode touches the continuum, resulting in strong continuum damping. However, unlike GTC, which is an initial value code, the eigenvalue code NOVA yields numerous possible solutions. Only solutions exhibiting minimal instabilities are analyzed. Note that the mode spatial structures and poloidal harmonics from NOVA are represented by the plasma radial displacement ($\xi$) while GTC solutions are expressed in terms of the electrostatic potential perturbation ($\delta\phi$). The two can be linked through their definitions of fields[34]:

NOVA:

$$\delta B = \nabla \times (\xi \times B_0),\ \delta E = -\partial_t \xi \times B_0 \tag{12}$$

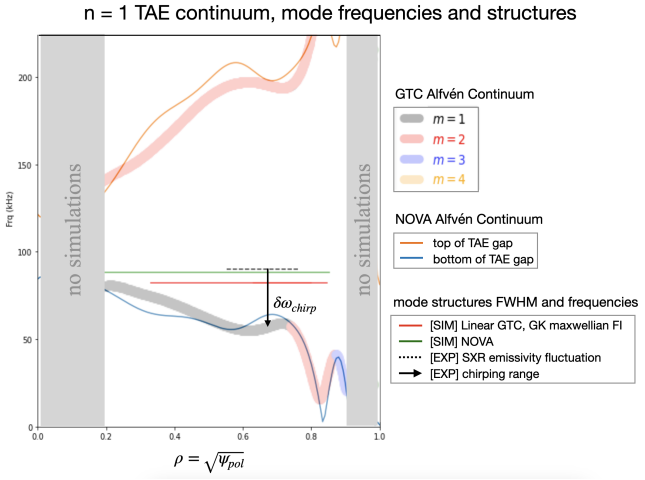


FIG. 5. mode structure FWHM from measurement (dashed line), NOVA (green line) and GTC (red line) together with Alfvén continuum in the range of TAE gap generated by GTC and NOVA calculated for MAST pulse 26887, t = 180ms.

GTC:

$$\delta B = \nabla \times (\delta A_{||} b_0),\ \delta E = -\nabla \delta\phi - \partial_t \delta A_{||} b_0 \tag{13}$$

Ideal MHD simulations are conducted using the NOVA code to establish a baseline for the other simulations reported in this paper. NOVA simulations on TAEs in NSTX have been validated and reported numerous times[3536], yielding solutions that agree with the frequency and radial mode structure at the linear stage (without or at the beginning of frequency chirping) of the mode. Using NOVA, a cluster of n = 1 TAE solutions in MAST near 90 kHz (in the lab frame) is identified, consistent with the frequency measured by OMAHA before chirping occurred in MAST shot 26887 at approximately 181 ms. The radial mode structures and poloidal harmonics are similar among the cluster of solutions, with $m = 1,2$ dominating and peaking near the $q = 1.5$ surface near $\rho = 0.6$, shown in figure 6. This agrees well with analytic theory in the large aspect ratio limit, which indicates that TAE peaks at the $q = \frac{m+1/2}{n}$ surface[37].

## V. ANTENNA-EXCITED TAES IN GTC

Eigenmodes excited by antennas are used to determine mode frequencies and damping rates in single- and two-fluid ideal MHD and linear GK regimes in GTC. In GTC, the antenna inserts an additional synthetic potential ($\phi_{ant}$) into the inductive potential: $\phi_{ind} = \phi_{eff} - \delta\phi + \phi_{ant}$, with $\phi_{ant}$ represented as a standing sinusoidal signal[38]:

$$\phi_{ant} = \phi_{ant,0}(\zeta,\theta,x)\cos(\omega_{ant} t) \tag{14}$$

, where $\zeta$ and $\theta$ are toroidal and poloidal angles, respectively, and the antenna spatial profile $\phi_{ant,0}(\zeta,\theta,x)$ is defined as fol-

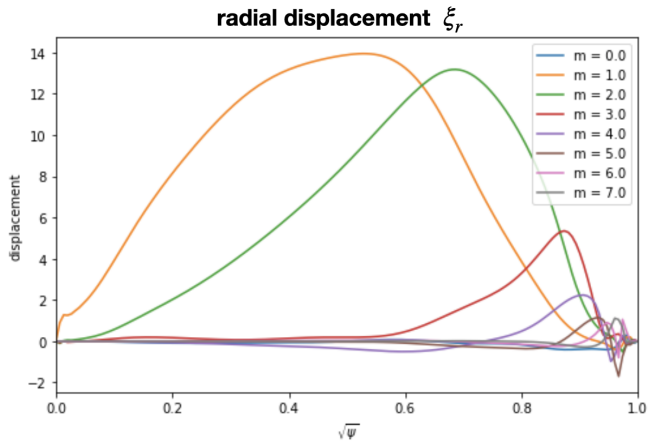


FIG. 6. Radial displacement of TAE at ≈89kHz from NOVA calculated for MAST pulse 26887, t = 180ms.

lows:

$$\phi_{ant,0} = \begin{cases} C_{amp}\left(\frac{exp\left(\frac{x-x_{ctr}}{2\sigma_w}\right)^2}{(1-exp\left(\frac{-x_{bd}}{2\sigma_w}\right)^2)} - exp\left(\frac{-x_{bd}}{2\sigma_w}\right)^2\right) cos(m\theta - n\zeta), & \text{if } |x-x_{ctr}| < x_{bd} \\ 0 & \text{otherwise} \end{cases} \quad (15)$$

, where $x \in [0,100]$ is the radial grid in GTC simulations, $C_{amp} = 10^{-4}$ is the antenna amplitude, $x_{ctr} = 70$ is the radial location of peak antenna amplitude in the GTC grid set near the $q = 1.5$ surface, $x_{bd} = 20$ is the radial size of the antenna in the GTC grid, and the width $\sigma_w = x_{bd}/2$. The experimental modes were not antenna driven. Hence the purpose of exciting the TAE with an antenna is to accurately measure the mode frequencies and damping rates without influences from numerical instabilities near boundaries, instead of aiming to recover the global radial mode structure computed by NOVA or measured by SXR. Hence the radial extent of the antenna envelope ($x_{bound} = 20$) is limited to region around $q = 1.5$ only to ensure that no modes or instabilities other than the n = 1, m = 1 TAE are excited by the antenna.

The excited mode will follow one of two scenarios. If the antenna frequency matches the TAE eigen-frequency, the mode will grow linearly up to the amplitude where the plasma damping balances with the antenna driving. Otherwise, the mode intensity grow with oscillations due to the frequency mismatch and saturate at a lower amplitude. The relationship between saturated intensity, antenna frequency, eigen-frequency, and damping rate follows the driven resonant cavity theory[39]:

$$A^2 \propto \frac{1}{(\omega_E^2 + \gamma_D^2 - \omega_{ant}^2)^2 + 4\gamma_D^2\omega_{ant}^2} \quad (16)$$

, where $\omega_E$ is the eigen-frequency, $\gamma_D$ is the damping rate, and $A^2$ is the normalized saturated intensity. This relation indicates that the mode would exhibit the strongest $A^2$ when $\omega_E = \omega_{ant}$ for a fixed $\gamma_D$. TAEs exist in the continuum gap, hence a resonant cavity model is used instead of a regular driven-damped mode model. The decay of the mode begins after the antenna is turned off, where $\gamma_D$ and $\omega_E$ can be measured by fitting the decaying oscillator function: $A(t) \propto e^{i\omega_E t} e^{\gamma_D t}$.

The mode eigen-frequency, damping rate due to continuum damping and the ratio of polodial harmonics are determined using the antenna module in single-fluid run modes in GTC. A TAE with $n = 1$, $m = 1,2$ is expected peak near the $q = 1.5$ surface. Therefore, $\phi_{ant,0}$ is positioned near $|q| = 1.5$ with mode numbers $n = 1$ and $m = 1$ in the antenna excitation of TAE. The single-fluid run mode has $\phi_{eff} = 0$ and hence $\delta E_{||} = 0$. The antenna is kept on until the amplitude of the excited mode is saturated, then the antenna is turned off to measure an eigen-frequency of 70.1 kHz, suggesting a TAE eigen-frequency close to 80 kHz after considering the plasma rotation frequency of about 10 kHz in this case. This frequency is about 8kHz (or 10 %) lower than the value predicted by NOVA and the initial frequency of the TAE. But it is interesting to note that the frequency from GTC matches closely the expected large aspect ratio ideal MHD (n,m) = 1,1 TAE frequency ($c_A/2qR$). The damping rate is measured to be $\gamma_D = -(2\pi) * 3342\,s^{-1}$ and $\gamma_D/\omega = -4.77\%$. The antenna-excited m = 1 harmonic closely resembles the results from ideal MHD NOVA, as shown in Figure 8 (a1)(a2), but the m = 2 harmonic has a much lower contribution to the overall mode structure in GTC compared to NOVA. Non-perturbative effects or differences in the treatments for equilibrium could contribute to the discrepancies in the mode frequency and the ratio of polodial harmonic. Contributions from reverse shear Alfvén eigenmodes (RSAEs) might also cause these discrepancies. RSAEs generally have eigen-frequencies in the range below the TAE frequency with only a single poloidal harmonic peaking near the $q_{min}$ in a reversed shear ($|q_0| > |q_{min}|$) plasma. However, RSAEs could be in an intermediate regime with both characteristics of TAEs and RSAEs, which have two coupled poloidal harmonics and in an intermediate frequency[40]. The equilibrium used in GTC simulations is slightly reversed shear with $q_{min}$ location ($\rho \approx 0.45$) not too far away from the $q = 1.5$ surface at $\rho \approx 0.7$ . Hence it is possible to have small contributions of m = 1 RSAE excited alongside m = 1, m = 2 TAE in GTC, and alter the overall mode eigen-frequency and the ratio of polodial harmonics from a conventional TAE.

The mode exhibits a similar eigen-frequency and greater damping rate when radiative damping is included in GTC. The mode is excited with the same antenna setting but in the two-fluid model with finite $\delta E_{||}$. The eigen-frequency of the mode at 72 kHz (before considering the rotation-induced Doppler shift) is similar to that found in the single-fluid MHD simulation. The relative amplitude of m = 1 and m = 2 $\delta\phi$ near the $|q| = 1.5$ surface is similar to that found in the single-fluid MHD simulation. However, $\delta\phi$ is weaker at $q_{min}$ in the two-fluid simulation (Figure 8 (b1)(b2)), suggesting that the mode could not be excited far away using the same $|q| = 1.5$ localized antenna profile that was used in the single fluid MHD simulation when radiative damping caused by the finite $\delta E_{||}$ is taken into account. The mode damping rate measured at $|q| = 1.5$ after the antenna is turned off is greater ($\gamma_{tot}/\omega = -4.77\%$ versus $-5.97\%$, as shown in Table I), also as a result of the $\delta E_{||}$ introduced by radiative damping.

Antenna-excited TAEs saturate at much lower amplitude

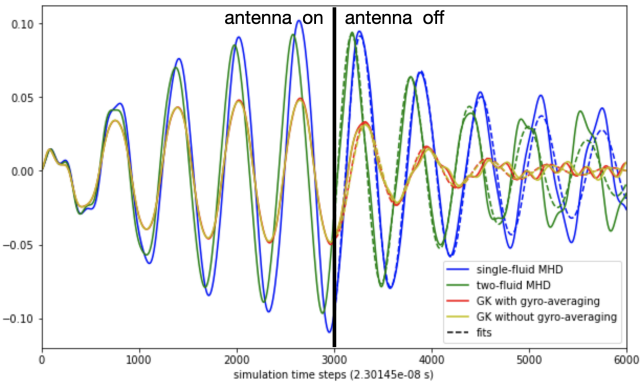


FIG. 7. The waveform (solid curves) of (n,m) = (1,1) near |q| = 1.5 of the antenna excited modes, with their $e^{i\omega_E t}e^{\gamma_D t}$ fits (dashed curves) for the period after the antenna was turned off

and exhibit significantly greater damping rate when kinetic thermal ions are included in GTC. The TAE is excited by the antenna in the same way as before but now with full-kinetic thermal ions, with finite $\delta E_{||}$ and without gyro-averaging. Thus, continuum, radiative, and ion Landau damping mechanisms are all included in this run mode. The eigen-frequency is found to be slightly lower than in the previous cases, 69.3 kHz before Doppler shift. Its mode structure and poloidal harmonics (Figure 8 (c1)(c2)) are similar to the two-fluid MHD case near $|q| = 1.5$. However, the damping rate at $|q| = 1.5$ after the antenna is turned off is more significant at $\gamma_D/\omega = -11.0\%$, most likely due to the addition of ion Landau damping similar to that found in RSAE cases in DIII-D[6]. The saturated amplitude is much lower compared to previous ideal MHD cases, as shown in figure 7. This is likely due to the more significant damping rate and agree with the resonant cavity mode model (Equation 16). The simulation can also include gyrokinetic thermal ions with gyro-averaging, which introduces the FLR effect. However, the saturated amplitude, eigen-frequency and damping rate in the gyro-averaging case are nearly the same as the full-kinetic case, suggesting that ion Landau damping is responsible for most of the additional damping rather than the FLR effect in gyro-kinetic simulation. Besides the differences in the net damping rates, the ion Landau damping might also affect the spatial structures of the modes. The ion Landau effect is the strongest when the phase velocities ($v_{phase,ion}$) of the ions approach $\omega_E/k_{||}$ where $k_{||} = (n - m/q)/R$ (in the large aspect ratio limit) is the parallel wave vector. The $T_i$ is at its maximum near the core (as shown in Figure 3(b)), suggesting that $v_{phase,ion}$ is likely to be closest to $\omega_E/k_{||}$ in the region and hence that ion Landau effect is the strongest near the core. As a result, the mode has a much weaker $\delta\phi$ in the core region ($\rho < 0.5$) in the simulation that includes gyro-kinetic thermal ions compared to the $\delta\phi$ from single-fluid simulation (Figures 8(c1)(c2) vs. (a1)(a2), respectively).

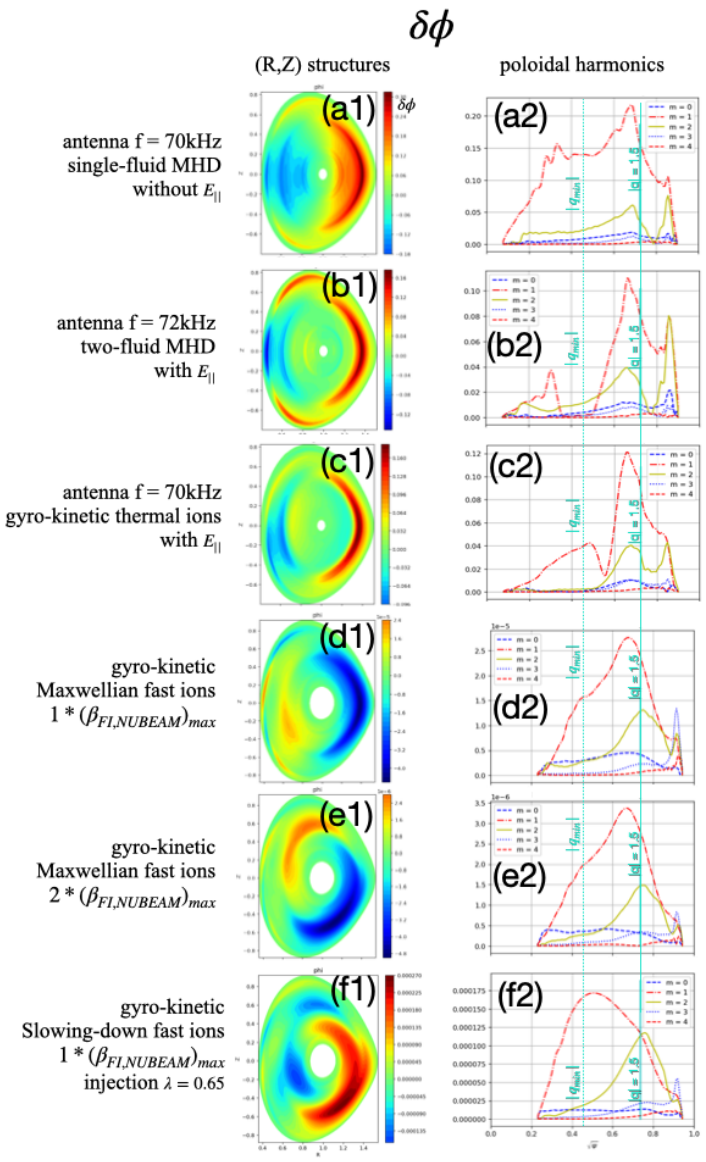


FIG. 8. 2D (R,Z) snapshots from GTC runs that excite n = 1 TAE with (a1) 70kHz antenna in single-fluid MHD plasma without $\phi_{eff}$; (b1) 72kHz antenna in double-fluid MHD plasma with $\phi_{eff}$;(c1) 70kHz antenna with gyro-kinetic thermal ions and $\phi_{eff}$; (d1) analytic Maxwellian fast ion profile with $1 * (\beta_{FI,NUBEAM})_{max}$, (e1) analytic Maxwellian fast ion profile with $2 * (\beta_{FI,NUBEAM})_{max}$, (f1) analytic fast ion slowing-down distribution with injection $\lambda = 0.65$. (a2) - (f2) show the corresponding poloidal harmonics m = [0,4]

## VI. TAES EXCITED BY MAXWELLIAN AND SLOWING-DOWN FAST ION DISTRIBUTIONS IN GTC

TAEs can also be excited by Maxwellian fast ion distributions in GTC as described in Equation 4. Analytic fast ion density profiles are employed to excite TAEs in the linear GK regime in GTC and reveal the instability threshold of the mode. The experimental fast ion distributions induced by NBI are computed by NUBEAM[30]. Spatial profiles of fast

ion temperature and density are considered, while their pitch and energy distributions are neglected for modes excited by Maxwellian distributions. Analytic fast ion density profiles with scales of 1, 1.5, 2, and 2.5 times the maximum fast ion density computed with NUBEAM ($(n_{FI,NUBEAM})_{max}$) are used in linear GTC runs to determine the instability threshold of the targeted TAE. The increase of the fast ion density scale factor subsequently increases the $\beta_{FI}$ and keep $T_{FI}$ unchanged in the scan. The TAE is marginally unstable when it is excited with $(\beta_{FI,sim})_{max} = 1 * (\beta_{FI,NUBEAM})_{max}$, indicating that the instability threshold is slightly below the maximum fast ion pressure reproduced by NUBEAM. The ratio of the net growth rate ($\gamma_{tot} = \gamma_L + \gamma_D$) to the mode frequency ($\omega$) for modes excited by 1, 1.5, 2, and 2.5 times $(\beta_{FI,NUBEAM})_{max}$ are 3.63%, 7.56%, 9.52%, and 11.77%, respectively, as shown in Figure 9 (a). The $\gamma_{tot}/\omega$ appears to be nearly linearly proportional to $\beta_{FI}$, which is similar to the approximation for low-n TAEs in large aspect ratio discussed in the Equation 10 of[37], despite in the low aspect ratio and with a significantly greater $\beta_{FI}/\beta_i$.

The frequencies of modes excited by the analytic fast ion profile with different pressure scales are similar. Previous benchmarks of GTC have demonstrated non-perturbative kinetic contributions from fast ions[38], resulting in differences in mode frequency compared to eigen-frequencies found in antenna scans without $\delta E_{||}$. The frequencies of modes excited by a fast ion profile with the pressure at 1 times $(\beta_{FI,NUBEAM})_{max}$ peak near 72 kHz before Doppler shift. The frequencies shift downward in cases when the $(\beta_{FI,NUBEAM})_{max}$ is scaled up, as shown in Figure 9 (b). The shift could be the result of the significantly increased fast ion density in the cases with higher fast ion pressure scales that alter the equilibrium when quasi-neutrality is considered, in addition to kinetic effects. The spatial structure of the modes excited by profiles with these scales is similar when they are in the exponential growth phase. The $\delta\phi$ peaks near $|q| = 1.5$ (Figure 8 (d1)(e1)) with $m = 1$ dominating the poloidal harmonic (Figure 8 (d2)(e2)). The contributions from $m = 2$ are more pronounced compared to the antenna-excited modes. However, the ratio of $m = 2$ to $m = 1$ is still not as much as those in ideal MHD NOVA, even when both are converted to the same physical quantity $\delta B_r/B$ for comparisons, as shown in Figure 10. The ratio of $m = 2$ to $m = 1$ ($(\delta B_{r,m=2})_{max}/(\delta B_{r,m=1})_{max}$)) in the GTC solution is lower than the NOVA solution ( $\approx 0.68$ versus $\approx 0.92$, respectively). This suggests that there are still contributions from m = 1 RSAE to the overall mode structure and frequency, similar to the antenna-excited cases.

Apart from Maxwellian distributions, analytic fast ion slowing-down distributions can be utilized to excite TAEs in GTC as described in Equation 7. Although the model does not accommodate the rapidly changing birth pitch across different major radii in spherical tokamaks as shown in Figure 4(a) in Section III, it is sufficient to represent most of the beam-induced fast ions as they are generated near $R \approx 1.1$ m with birth pitch variable concentrated near $\lambda = 0.65$. Hence, analytical slowing-down distributions that fit the fast ion pitch-energy distributions there (Figures 4(b)(c)) could realistically represent the trapped particles interacting with the TAE.

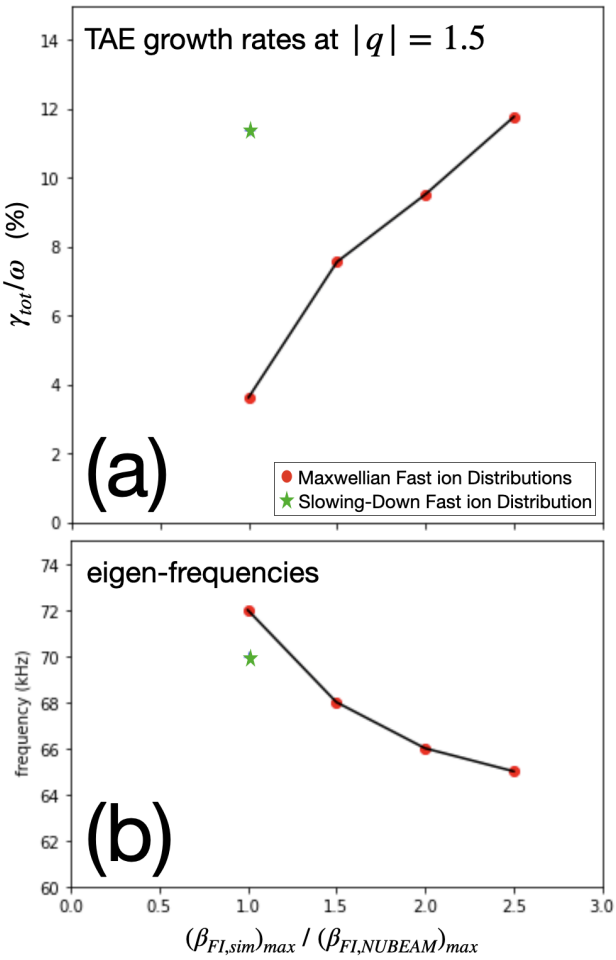


FIG. 9. (a) growth rates and (b) eigen-frequencies (in the plasma frame) of n = 1, m = 1 TAEs excited by analytic Maxwellian fast ion $\beta_{FI}$ of 1, 1.5, 2 and 2.5 times of $(\beta_{FI,NUBEAM})_{max}$ (by scaling $n_{FI}$), sampled near |q| = 1.5 surface

The TAE driven by the analytic slowing-down fast ion distribution exhibits a higher growth rate and slightly different mode spatial structure compared to modes excited by Maxwellian distributions, probably due to the anisotropic distribution of fast ions[41]. The radial fast ion density and temperature (for determining $v_c$ and $v_0$) profiles are taken from the Maxwellian fast ion case with $(\beta_{FI,sim})_{max} = 1 * (\beta_{FI,NUBEAM})_{max}$ for consistency. The frequencies of modes from the two cases remain similar to those of the mode excited solely by the Maxwellian distribution, around 70 kHz before a Doppler shift correction. However, the growth rate of the mode excited by the slowing-down distribution $(n,m) = (1,1)$ is significantly higher ($\gamma_{tot}/\omega = 10.75\%$) than the mode excited solely by the Maxwellian distribution using the same fast ion pressure profiles. This indicates that the mode becomes more unstable with the use of the slowing-down distribution, probably due to the anisotropic fast ion distributions peak at higher $\lambda$, providing more fast ions to be in shear Alfvén resonance. The effects of fast ion anisotropy on the

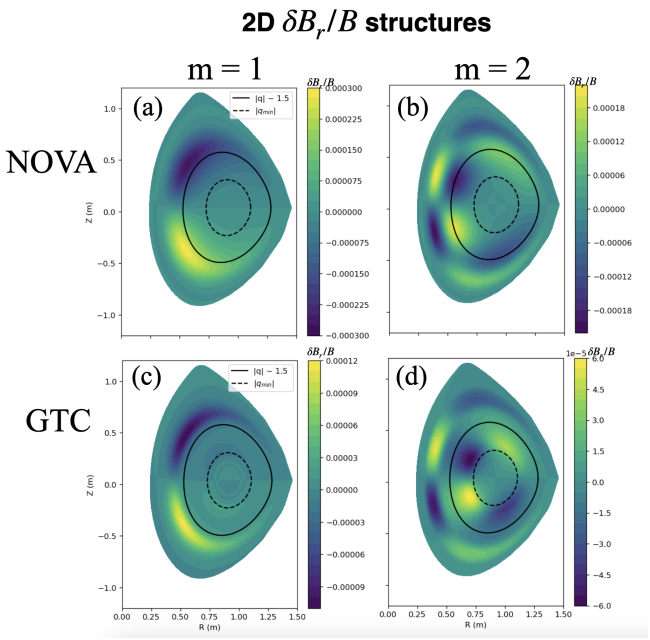


FIG. 10. 2D (R,Z) $\delta B_r/B$ structures of (a) m = 1 and (b) m = 2 from NOVA; (c) m = 1 and (d) m = 2 from linear GTC with the mode excited by analytic Maxwellian fast ion $\beta_{FI}$ of $3*(\beta_{FI,NUBEAM})_{max}$ (by scaling $n_{FI}$)

growth rate had also been observed in the stability study of TAEs in ITER scenarios when the pitch distribution is considered in the kinetic-MHD code NOVA-K[3]. The difference of TAE growth rates between fast ion Maxwellian and slowing down distributions excited modes with the same $n_{FI}$ in GTC, however, is greater than those found using NOVA/-K. The discrepancy could be the result of additional kinetic effects included in GTC compared to NOVA/-K, and also the differences in fast ion beta and aspect ratio in MAST case compared to the ITER case discussed in[3].

The use of an analytic slowing-down distribution in GTC also alters the radial structure of the mode compared to the case with Maxwellian distribution excitation. The peak of the $m = 1$ component in $\delta\phi$ shifts to $\rho = 0.5$ close to $|q_{min}|$ (Figure 8 (f2)) from $\rho = 0.65$ near $|q| = 1.5$ in cases excited solely by the Maxwellian distributions. In the slowing-down case, the ratio of the $m = 1$ to $m = 2$ component in $\delta\phi$ is comparable at $|q| = 1.5$, but $m = 1$ is dominant near the $|q_{min}|$. Additionally, a spiral feature emerges in the 2D $(R,Z)$ structure of $\delta\phi$ for the mode excited by the $\lambda = 0.65$ slowing-down distribution (Figure 8 (f1)), absent in the mode excited by the Maxwellian distribution alone. This spiral suggests a stronger $k_r$, implying more significant radial energy transfer than the previous case. These characteristics suggest the use of an anisotropic fast ion distribution causes the mode to exhibit distinctive features of both TAE at $q = 1.5$ and RSAE at $q_{min}$, rather than the ambiguous structures seen in previous cases. This is probably due to the differences in $\nabla f_{0f}/f_{0f}|_\mu$ (Equation 8) and $(1/f_{0a})(\partial f_{0a}/\partial v_{||})$ (Equation 9) peaking locations when the pitch of fast ions is considered, making both m = 1 RSAE and m = 1,2 TAE more distinguishable at their associated $q$ surfaces.

## VII. SUMMARY

Linear gyrokinetic simulations for TAEs in the MAST discharge 26887 at 180 ms were conducted using various GTC run modes to explore different driving and damping mechanisms, as summarized in Table I. These simulations demonstrate GTC's capability to incorporate various mechanisms that significantly affect the TAE, which are absent in MHD models. Antenna-driven TAEs in single-fluid (without $\delta E_{||}$) and two-fluid (with $\delta E_{||}$) plasma in GTC are subject to similar damping rates of about 5-6%. This indicates that radiative damping introduced by the two-fluid model does not significantly increase the damping beyond the continuum level. However, the damping rate increases significantly to 11% when the thermal ions are in the gyrokinetic regime, which includes the ion Landau effect. On the other hand, the damping rate only changes slightly when FLR effects are included, introduced by the gyro-averaging of the thermal ions. This suggests that the ion Landau effect, which is absent in ideal MHD codes, makes the most significant contribution to the mode damping rate.

TAEs excited by Maxwellian fast ion distributions with various fast ion pressures in GTC demonstrate the sensitivity of TAE growth rates to the fast ion gradient. A scan of analytic fast ion profiles with densities ranging from 1 to 2.5 times the level computed by NUBEAM was conducted. The spatial structures of these TAEs are similar to each other and to NOVA ideal MHD eigenmode calculations, with comparable proportions of $m = 1$ and $m = 2$ components in $\delta\phi$. The TAEs excited in the fast ion density scan have growth rates ranging from 3.9 to 16.1%. This indicates that the experimental fast ion density computed by NUBEAM is sufficient to drive the mode and suggests that the stability threshold lies between 0.5 and 1 times the NUBEAM fast ion density.

Fast ion anisotropy can significantly affect the stability of TAEs. Besides fast ion Maxwellian distributions, GTC can also be used to model the excitation of TAEs with analytic slowing-down fast ion distributions. The growth rate increases significantly to about 11% when an analytic slowing-down distribution that mimics the NUBEAM fast ion pitch/energy distribution near the peak fast ion density ($R \approx 1.1$m) with the same analytic fast ion density profile used in the Maxwellian case is used to excite the mode. This demonstrates that mode stability is sensitive to the pitch and energy distribution of the beam-induced fast ions. The $m = 1$ and $m = 2$ components at $q = 1.5$ are similar to the previous case excited solely by the Maxwellian distributions, but $m = 1$ $\delta\phi$ extends further to the core near the $q_{min}$ location. A more noticeable spiral 2D structure, implying a stronger $k_r$ compared to the mode excited by the Maxwellian distribution, appears in the mode excited by the slowing-down distribution. This suggests that additional contributions from an RSAE are present due to the differences in $\nabla f_{0f}/f_{0f}$ peaking locations arising from the replacement of a Maxwellian distribution with an anisotropic

slowing-down distribution.

Overall, the GTC simulation results are in good agreement with the measurements. Despite different representations of thermal and fast ions, the eigen-frequencies of TAEs excited in various GTC run modes fall within a narrow range of 69 to 72 kHz. The laboratory frame frequencies are close to 80 kHz after accounting for the $\approx$ 10kHz plasma rotation Doppler shift. This is about 9% lower than the frequency computed by NOVA and the measured initial frequency of the targeted chirping TAE. Interestingly, the frequencies from GTC are closer to the TAE frequency at its peak mode amplitude, as well as to the ideal MHD value for the $(n,m) = (1,1)$ TAE frequency, once the rotation Doppler shift is considered. The discrepancy could be attributed to non-perturbative effects, considering similar differences between NOVA and GTC ideal MHD run modes. However, the results are still in good agreement as they remain within the frequency range of the chirping TAE. The radial mode structures from the GTC simulations that include fast ions also align with experimental results inferred from tangential SXR. The $\delta\phi$ from these simulations all peak around $\rho = 0.6$ to 0.8, close to the expected mode location for ideal MHD $n = 1$ and $m = 1,2$ TAEs, as well as the measured SXR $\delta\varepsilon$. Discrepancies in these simulations are found only when the poloidal structures and harmonics are considered, possibly due to the treatment of fast ion distributions (whether they are Maxwellian or anisotropy) in these simulations. However, the results from these simulations are equivalent when compared with the mode structure measurements as neither poloidal structures nor harmonics are measured or inferred from the suite of available diagnostics presented in this paper. Future experimental efforts could focus on directly inferring fast ion anisotropy using tomography techniques[42] and on measuring poloidal mode structures and harmonics with poloidally viewing diagnostics. These efforts could provide valuable references for detailed comparisons between Maxwellian and anisotropic fast ion models used in the GTC in the future.

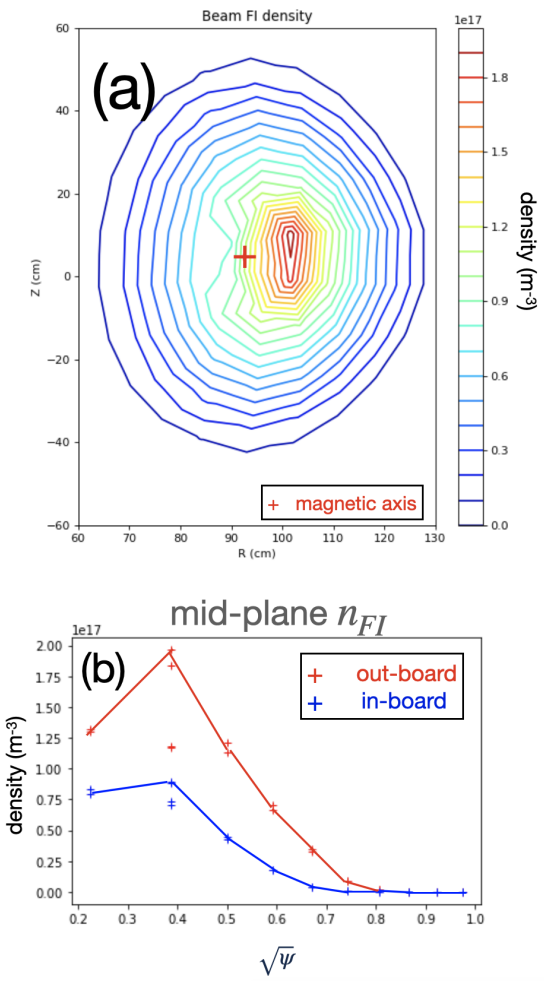


FIG. 11. (a) 2D and (b) mid-plane radial fast ion density profiles from NUBEAM/TRANSP

## ACKNOWLEDGEMENTS

The authors would like to thank the organizers of 30th ITPA Topical Group Meeting on Energetic Particle Physics, where useful discussions with participants took place. The authors also thank Michael Fitzgerald, Sergei Sharapov and Nikolai Gorelenkov for useful discussions and suggestions on the properties of TAEs in STs. The authors would like to express their appreciation for the efforts of MAST team for the physics campaigns and maintaining the measurements' database.

This material is based upon work supported by the US DoE [grant number DE-SC0019007], the SCGSR program administered by ORISE [grant number DE-SC0014664] and the RCUK [grant number EP/T012250/1].

### Appendix A: Two-dimensional fast ion density profiles

The two-dimensional (R,Z) fast ion density distribution peaks in the outboard region and lacks poloidal symmetry. Consequently, the fast ion pressure gradient is highest in the outboard region, with the peak outboard fast ion pressure gradient occurring near $\rho_{out} = 0.5$, as shown in Figure 11(a). However, GTC can only handle poloidally symmetric fast ion density profiles, and using the poloidally averaged NUBEAM density profile leads to an insufficient pressure gradient to drive the TAE, especially considering that ballooning modes are more sensitive to the outboard pressure than the inboard region. Therefore, an analytic profile with the maximum gradient peaking at $\rho = 0.6$ (as shown in Figure 3(a)), which is close to $q = 1.5$ and similar to the outboard fast ion density profile shown in Figure 11(b), is used in GTC simulations.

[1]Z. Lin, T. S. Hahm, W. W. Lee, W. M. Tang, and R. B. White, "Turbulent transport reduction by zonal flows: Massively parallel simulations," Science **281**, 1835–1837 (1998).
[2]K. Ikeda, "Progress in the iter physics basis," Nuclear Fusion **47** (2007), 10.1088/0029-5515/47/6/e01.
[3]N. Gorelenkov, H. Berk, and R. Budny, "Beam anisotropy effect on alfvén eigenmode stability in iter-like plasmas," Nuclear Fusion **45**, 226–237 (2005).
[4]P. Liu, X. Wei, Z. Lin, G. Brochard, G. Choi, W. Heidbrink, J. Nicolau, and G. McKee, "Regulation of alfvén eigenmodes by microturbulence

in fusion plasmas," Physical Review Letters **128** (2022), 10.1103/physrevlett.128.185001.

[5]D. A. Spong, E. M. Bass, W. Deng, W. W. Heidbrink, Z. Lin, B. Tobias, M. A. Van Zeeland, M. E. Austin, C. W. Domier, and N. C. Luhmann, "Verification and validation of linear gyrokinetic simulation of alfvén eigenmodes in the diii-d tokamak," Physics of Plasmas **19** (2012), 10.1063/1.4747505.

[6]W. Deng, Z. Lin, I. Holod, Z. Wang, Y. Xiao, and H. Zhang, "Linear properties of reversed shear alfvén eigenmodes in the diii-d tokamak," Nuclear Fusion **52**, 043006 (2012).

[7]W. Deng, Z. Lin, and I. Holod, "Gyrokinetic simulation model for kinetic magnetohydrodynamic processes in magnetized plasmas," Nuclear Fusion **52**, 023005 (2012).

[8]M. Cox, "The mega amp spherical tokamak," Fusion Engineering and Design **46**, 397–404 (1999).

[9]J. Rivero-Rodríguez, K. McClements, M. Fitzgerald, S. Sharapov, M. Cecconello, N. Crocker, I. Dolby, M. Dreval, N. Fil, J. Galdón-Quiroga, M. García-Muñoz, S. Blackmore, W. Heidbrink, S. Henderson, A. Jackson, A. Kappatou, D. Keeling, D. Liu, Y. Liu, C. Michael, H. Oliver, P. Ollus, E. Parr, G. Prechel, T. Rhodes, D. Ryan, P. Shi, M. Vallar, L. Velarde, T. Williams, and H. Wong, "Overview of fast particle experiments in the first mast upgrade experimental campaigns," Nuclear Fusion **64**, 086025 (2024).

[10]N. Chulu Chinn, F. Palermol, B. McMillan, C. Roach, M. Fitzgerald, K. McClements, S. Blackmore, M. Dreval, A. Mishchenko, and T. Hayward-Schneider, "Gyrokinetic investigation of tae damping channels with comparison to theory and application to mast-u," — **(to be submitted)** (2024).

[11]C. Z. Cheng and M. S. Chance, "Low-n shear alfvén spectra in axisymmetric toroidal plasmas," The Physics of Fluids **29**, 3695–3701 (1986).

[12]I. Holod, W. L. Zhang, Y. Xiao, and Z. Lin, "Electromagnetic formulation of global gyrokinetic particle simulation in toroidal geometry," Physics of Plasmas **16**, 122307 (2009).

[13]A. J. Brizard and T. S. Hahm, "Foundations of nonlinear gyrokinetic theory," Reviews of Modern Physics **79**, 421–468 (2007).

[14]F. Zonca and L. Chen, "Resonant and non-resonant particle dynamics in alfvén mode excitations," Plasma Physics and Controlled Fusion **48**, 537–556 (2006).

[15]X. Wang, S. Briguglio, L. Chen, C. Di Troia, G. Fogaccia, G. Vlad, and F. Zonca, "An extended hybrid magnetohydrodynamics gyrokinetic model for numerical simulation of shear alfvén waves in burning plasmas," Physics of Plasmas **18** (2011), 10.1063/1.3587080.

[16]W. Gekelman, S. Vincena, B. Van Compernolle, G. J. Morales, J. E. Maggs, P. Pribyl, and T. A. Carter, "The many faces of shear alfvén waves," Physics of Plasmas **18**, 055501 (2011).

[17]D. Moseev and M. Salewski, "Bi-maxwellian, slowing-down, and ring velocity distributions of fast ions in magnetized plasmas," Physics of Plasmas **26** (2019), 10.1063/1.5085429.

[18]P. H. Rebut and B. E. Keen, "The jet experiment: Evolution, present status, and prospects," Fusion Technology **11**, 13–42 (1987).

[19]L. C. Appel and M. J. Hole, "Calibration of the high-frequency magnetic fluctuation diagnostic in plasma devices," Review of Scientific Instruments **76** (2005), 10.1063/1.2009107.

[20]M. J. Hole and L. C. Appel, "A modulation model for mode splitting of magnetic perturbations in the mega ampere spherical tokamak," Plasma Physics and Controlled Fusion **51**, 045002 (2009).

[21]L. Lao, H. St. John, R. Stambaugh, A. Kellman, and W. Pfeiffer, "Reconstruction of current profile parameters and plasma shapes in tokamaks," Nuclear Fusion **25**, 1611–1622 (1985).

[22]L. Lao, J. Ferron, R. Groebner, W. Howl, H. St. John, E. Strait, and T. Taylor, "Equilibrium analysis of current profiles in tokamaks," Nuclear Fusion **30**, 1035–1049 (1990).

[23]L. Appel and I. Lupelli, "Equilibrium reconstruction in an iron core tokamak using a deterministic magnetisation model," Computer Physics Communications **223**, 1–17 (2018).

[24]I. H. Hutchinson, *Principles of Plasma Diagnostics* (Cambridge University Press, 2002).

[25]H. Wong, S. Blackmore, C. Michael, K. McClements, C. N.A., M. Fitzgerald, L. Garzotti, R. Scannell, S. Thomas, D. Dunai, A. Field, A. Jackson, M. Podesta, J. Rivero-Rodriguez, M. Cecconello, A. Sladkomedova, and T. Carter, "Fishbone instabilities and the impacts on core confinement in mast and mast-u," Nuclear Fusion **(submitted and awaiting for peer review)** (2024).

[26]K. G. McClements, J. Young, L. Garzotti, O. Jones, and C. A. Michael, "Abel inversion of soft x-ray fluctuations associated with fast particle-driven fishbone instabilities in MAST plasmas," Plasma Research Express **3**, 034001 (2021).

[27]S. Henderson, "Impurity transport studies on mast," PhD Thesis (2014).

[28]K. G. McClements, M. P. Gryaznevich, S. E. Sharapov, R. J. Akers, L. C. Appel, G. F. Counsell, C. M. Roach, and R. Majeski, "Physics of energetic particle-driven instabilities in the start spherical tokamak," Plasma Physics and Controlled Fusion **41**, 661–678 (1999).

[29]J. Breslau, M. Gorelenkova, F. Poli, J. Sachdev, A. Pankin, G. Perumpilly, X. Yuan, and L. Glant, en"Transp," (2018).

[30]A. Pankin, D. McCune, R. Andre, G. Bateman, and A. Kritz, "The tokamak monte carlo fast ion module nubeam in the national transport code collaboration library," Computer Physics Communications **159**, 157–184 (2004).

[31]L. Spitzer, "Physics of fully ionized gases," Interscience, New York (1956).

[32]D. V. Sivukhin, "Coulomb collisions in a fully ionized plasma," Rev. Plasma Phys. (USSR)(Engl. Transl.) **Vol: 4** (1966).

[33]T. H. Stix, "Heating of toroidal plasmas by neutral injection," Plasma Physics **14**, 367–384 (1972).

[34]Z. Wang, Z. Lin, W. Deng, I. Holod, W. W. Heidbrink, Y. Xiao, H. Zhang, W. Zhang, and M. Van Zeeland, "Properties of toroidal alfvén eigenmode in diii-d plasma," Physics of Plasmas **22** (2015), 10.1063/1.4908274.

[35]N. N. Gorelenkov, E. Belova, H. L. Berk, C. Z. Cheng, E. Fredrickson, W. W. Heidbrink, S. Kaye, and G. J. Kramer, "Beam ion driven instabilities in the national spherical tokamak experiment," Physics of Plasmas **11**, 2586–2593 (2004).

[36]E. Fredrickson, N. Crocker, D. Darrow, N. Gorelenkov, G. Kramer, S. Kubota, M. Podesta, R. White, A. Bortolon, S. Gerhardt, R. Bell, A. Diallo, B. LeBlanc, F. Levinton, and H. Yuh, "Fast-ion energy loss during tae avalanches in the national spherical torus experiment," Nuclear Fusion **53**, 013006 (2012).

[37]G. Y. Fu and J. W. Van Dam, "Excitation of the toroidicity-induced shear alfvén eigenmode by fusion alpha particles in an ignited tokamak," Physics of Fluids B: Plasma Physics **1**, 1949–1952 (1989).

[38]W. Zhang, I. Holod, Z. Lin, and Y. Xiao, "Global gyrokinetic particle simulation of toroidal alfvén eigenmodes excited by antenna and fast ions," Physics of Plasmas **19** (2012), 10.1063/1.3685703.

[39]H. S. Zhang, Z. Lin, I. Holod, X. Wang, Y. Xiao, and W. L. Zhang, "Gyrokinetic particle simulation of beta-induced alfvén eigenmode," Physics of Plasmas **17** (2010), 10.1063/1.3498761.

[40]J. Bland and S. Sharapov, "Core-localized toroidal alfvén eigenmodes in spherical tokamaks," Fusion Engineering and Design **190**, 113694 (2023).

[41]G. Brochard, C. Liu, X. Wei, W. Heidbrink, Z. Lin, N. Gorelenkov, C. Chrystal, X. Du, J. Bao, A. Polevoi, M. Schneider, S. Kim, S. Pinches, P. Liu, J. Nicolau, and H. Lütjens, "Saturation of fishbone instability by self-generated zonal flows in tokamak plasmas," Physical Review Letters **132** (2024), 10.1103/physrevlett.132.075101.

[42]B. Madsen, M. Salewski, J. Huang, A. S. Jacobsen, O. Jones, and K. G. McClements, "Velocity-space tomography using prior information at mast," Review of Scientific Instruments **89** (2018), 10.1063/1.5035498.